Thermal Analysis of $LiNi_{0.4}Co_{0.2}Mn_{0.4}O_2$/Mesocarbon Microbeads Cells and Electrodes: State-of-Charge and State-of-Health Influences on Reaction Kinetics

S. Hildebrand,[1,2,=,*] A. Rheinfeld,[3,=,*,z] A. Friesen,[1] J. Haetge,[1] F. M. Schappacher,[1,z] A. Jossen,[3] and M. Winter[1,2,4,]**

[1]*MEET Battery Research Center, Westfälische Wilhelms-Universität Münster, D-48149 Münster, Germany*
[2]*Institute of Physical Chemistry, Westfälische Wilhelms-Universität Münster, D-48149 Münster, Germany*
[3]*Institute for Electrical Energy Storage Technology, Technical University of Munich, D-80333 Munich, Germany*
[4]*Helmholtz-Institute Münster, IEK-12, Research Center Jülich GmbH, D-48149 Münster, Germany*

The thermal stability of lithium ion batteries was studied by means of Accelerating Rate Calorimetry in Heat-Wait-Search operation on both electrode and cell level. Fresh and aged samples were investigated depending on the state-of-charge (SoC) of a 5 Ah pouch cell comprising mesocarbon microbeads and $LiNi_{0.4}Co_{0.2}Mn_{0.4}O_2$ as the anode and cathode materials. 1 M $LiPF_6$ in EC:DEC 3:7 (by weight) containing 2 wt% VC and 0.5 wt% LiBOB was chosen as the electrolyte. Measurements on the electrode level revealed a higher self-heating rate (SHR) of the cathode compared to the anode for all SoC and state-of-health (SoH) combinations in the temperature range where a self-sustaining decomposition reaction could be detected. A lower SoC showed a lower SHR of the electrode/electrolyte mixture with no reaction detected on the anode side $\leq$ 50% cell SoC. Cyclic aging led to a decrease in thermal stability of the cathode at lower SoC values with no significant influence on the anode implying a larger safety threat on the cell level. Avrami-Erofeev and autocatalytic reaction models were used to quantify the influences of SoC and SoH on reaction kinetics. Full cell measurements confirmed the observations at a higher SHR.
 [DOI: 10.1149/2.0361802jes]

Manuscript submitted November 13, 2017; revised manuscript received December 20, 2017. Published January 5, 2018.

Based on their high energy and power density combined with a long cycle life, high energy efficiency and low costs, lithium ion batteries are currently the state-of-the-art energy source for electric vehicles (EV).[1–3] A long cycle life requires excellent aging behavior, whereas a high energy and power density demands for a high level of safety in order to comply with automotive prerequisites.[4–6] Many studies have dealt with the investigation of aging and safety individually as well as their interplay.[4,7–13] Yet, these interactions are not fully understood. Accelerating Rate Calorimetry (ARC) has been reported to be a promising method to measure the thermal stability of samples under quasi-adiabatic conditions. This method can be applied from single battery materials[14–20] up to full cells.[11,13,21] Based on the prevailing quasi-adiabatic conditions, a worst-case scenario can be simulated. With no heat dissipation taking place, the generated heat can be evaluated by measuring the temperature increase of the sample, knowing its total heat capacity.[22] This behavior can be readily transferred to real life scenarios where heat dissipation during cell failure is partially inhibited by the cell surroundings.

Predicting a cell's behavior during thermal abuse conditions is a topic of major interest in order to prevent hazardous situations on the battery pack level such as the propagation of thermal runaway after a single cell failure.[23] Due to the complexity of cell thermal runaway dynamics influenced e.g. by material composition[14,15] and morphology,[24–26] modeling and simulation can help to identify the dominating processes and interactions within a single cell based on individual material decomposition reactions.[27–29] Characteristic kinetic parameters of predominantly empirical decomposition reaction models were reported to be determined via calorimetric measurements such as Differential Scanning Calorimetry (DSC) and ARC.[22]

Richard et al. started to use data of ARC Heat-Wait-Search (HWS) experiments in order to determine the activation energy of the reaction between a lithiated anode and the surrounding electrolyte for modeling and simulation purposes.[20,30] Further work in that direction was carried out to study the thermal decomposition reaction of delithiated cathodes containing $LiCoO_2$ (LCO).[14,31–33] These findings were the basis for numerous model implementations to describe the overall cell behavior during a thermal runaway[27,28,34] as well as its local effects.[35,36]

The work presented here focuses on studying the influences of a cell's state-of-charge (SoC) and state-of-health (SoH) on both the single electrode and the full cell thermal stability. In the first part of this work, ARC-HWS measurements are conducted and discussed on the electrode level. These findings are further correlated with X-ray powder diffraction (XRD) measurements in order to identify the underlying decomposition reaction mechanism within the cathode. In the second part of this work, the kinetics of the occurring decomposition reactions are investigated more closely by means of model based data analysis as previously suggested.[33] Based on this data analysis, influences of SoC and SoH on parameters of Arrhenius-type "kinetic triplets" are investigated. In the final part of this work, the identified reaction models are used to correlate the carried out ARC-HWS measurements on the electrode level with those conducted on the full cell level.

The studied electrode materials were harvested from medium sized (i.e. approximately 5 Ah) pouch type cells which were manufactured with the aid of an in-house laboratory scale manufacturing line. On the electrode level, two-component systems of composite electrode material and electrolyte (1 M $LiPF_6$ in ethylene carbonate (EC): diethyl carbonate (DEC) 3:7 (by weight) containing 2 wt% vinylene carbonate (VC) and 0.5 wt% lithium bis(oxalate)borate (LiBOB)) were examined individually. On the cell level, the corresponding pouch cells comprising electrodes with $LiNi_{0.4}Co_{0.2}Mn_{0.4}O_2$ (NCM-424, this work expressed as: NMC-442) as the cathode and mesocarbon microbeads (MCMB) as the anode active material were tested.

Experimental

Electrode manufacturing and cell assembly.—Pouch cells were assembled containing 18 cathode sheets (66 × 119 mm) and 19 anode sheets (68 × 121 mm) with the aid of an in-house laboratory scale manufacturing line. The composite electrode on the cathode side consisted of NMC-442 (BASF, Germany) as the active material, Super P (TIMCAL, Switzerland) as the conductive additive and polyvinylidene difluoride (PVdF) (Solvay, Belgium) as the binder with a mass ratio of 93:3:4. The resulting single-sided mass loading of the electrode after calendaring was 15 mg cm^{-2} at an average thickness of

=These authors contributed equally to this work.
*Electrochemical Society Member.
**Electrochemical Society Fellow.
zE-mail: alexander.rheinfeld@tum.de; falko.schappacher@uni-muenster.de

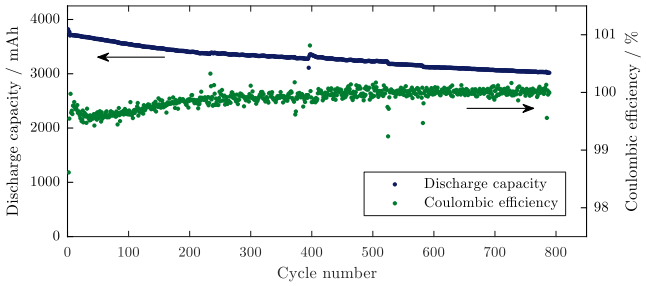

Figure 1. Cycling data of a 5 Ah pouch cell at 4C containing NMC-442 as cathode, MCMB as anode and a mixture of 1 M $LiPF_6$ in EC:DEC 3:7 (by weight) + 2 wt% VC and 0.5 wt% LiBOB as electrolyte, Data covers the first cycle after formation until the capacity faded to 80% of its initial capacity at 4C (i.e. 80% SoH, by definition in this work).

50 μm of the composite electrode. The slurry was cast on Al foil (15 μm thickness) as the current collector. The composite electrode on the anode side consisted of MCMB (10–28, Osaka Gas Chemicals, Japan) as the active material, hard carbon (Kureha, USA) and Super P (TIMCAL, Switzerland) as the conductive additives and PVdF (Solvay, Belgium) as the binder. The mass ratio was chosen as 83.2:9.3:0.5:7. The resulting single-sided mass loading of the electrode on the Cu current collector (10 μm thickness) was 10 mg cm^{-2} with an average thickness of 65.5 μm of the composite electrode after calendaring. A mixture of 1 M $LiPF_6$ in EC:DEC 3:7 (by weight) blended with 2 wt% VC and 0.5 wt% LiBOB (BASF, Germany) was used as the electrolyte. A Mitsubishi OZ-S30 polyester non-woven membrane with ceramic coating (30 μm thickness, Mitsubishi Paper Mills Ltd., Japan) was used as the separator.

Formation procedure.—The formation procedure consisted of five constant-current (CC) charge (first charge at 0.05C then at 0.1C) and discharge steps (0.1C) between 3.0 and 4.2 V at an ambient temperature of 20°C. The SoC was adjusted with a constant current step of 0.5C, followed by a constant voltage phase at 4.2 V until the current dropped below 0.05C (CC/CV, I < 0.05C) and the desired SoC was reached based on the discharge capacity of the previous cycle.

Aging procedure.—The aging procedure consisted of a sequence of a CC/CV (I < 0.05C) charge step to the charge voltage of 4.2 V followed by a CC discharge step until 3.0 V was reached. The charge and discharge steps were both performed at 4C in order to accelerate the aging procedure. The aging procedure was stopped at 80% SoH, whereas the SoH was defined by relating the discharge capacity at 4C to the discharge capacity at 4C of the third cycle after the formation procedure. This implies that the SoH determination chosen here includes effects of both capacity fade and resistance increase. The aging procedure as described was carried out at an ambient temperature of 20°C. Both the formation and cycling procedures were performed with the aid of a Series 4000 Battery Tester (Maccor, USA). Exemplary test data of cell aging is shown in Fig. 1. The cell shown was cycled for more than 750 cycles until the end-of-life criterion (i.e. 80% SoH) was reached. All cells cycled showed a similar aging behavior. Although at higher C-rates, accelerated aging phenomena like Li plating can occur during charging,[12,37,38] the discharge capacity faded without major drops during these cycles so that the aging process can be considered as fairly constant throughout the whole cycling procedure and therefore suitable for the carried out investigations. After cell opening, the cells also did not show any indication toward Li plating which supports this consideration. The same cells cycled at 1C showed comparable results, with a capacity fade to 80% after approximately 4000 cycles.

X-ray powder diffraction.—XRD measurements on the electrodes were performed on a D8 Advance Diffractometer (Bruker, Germany) with Cu K_α radiation ($\lambda = 0.154$ nm) equipped with a Lynxeye detector in order to investigate crystalline changes after aging. The diffractograms were measured with a step width of 0.021° 2Θ in the range of 15 to 90° 2Θ. A duration of 2 s per step was chosen.

ARC sample preparation.—For the ARC full cell measurements, the cells were placed in a stainless steel holder and were then transferred into the ARC. For the electrode measurements, the cells were first disassembled at the adjusted SoC within a dry room (dew point below −60°C). After the disassembly, the separated electrodes were transferred into a glove box (M. Braun Inertgas-Systeme GmbH, Germany) under argon atmosphere (6.0 purity, Westfalen Gas; O_2 < 0.1 ppm, H_2O < 0.1 ppm). Opening the 5 Ah pouch cells in a dry room environment before transferring the samples into a glove box was chosen for safety reasons as all cells were opened at a defined SoC which poses a certain risk to the personnel involved in the procedure. With this approach, necessary counter-measures could have been provided if the cell had been shorted during cell dismantling. The electrode sheets were then cut into pieces with a size of around 1 mm^2. Spherical titanium vessels (Netzsch, Germany) with a wall thickness of 0.5 mm, a volume of 1 mL and a mass of 3 g were filled with 0.7 mL of electrolyte and 0.7 g of composite electrode material. The Al and Cu current collectors were kept in the sample mixture and are generally considered as thermally inactive material. At least two ARC-HWS experiments were carried out per material, SoC and SoH combination.

ARC measurements.—ARC experiments on the electrode level were carried out with a standard Enhanced System Accelerating Rate Calorimeter (ES-ARC) manufactured by Thermal Hazard Technology (THT, UK) whereas for the cell level experiments, a larger ARC (EV-ARC) of the same manufacturer was used. A stainless steel holder was used for the full cell ARC-HWS experiments in order to guarantee a thermal contact between the pouch foil and the electrode stack throughout the duration of the experiments. A thermocouple was attached to the center of the cell's surface with the aid of Al tape. The spherical Ti vessels chosen for the two-component material tests guaranteed a gastight environment throughout the measurements. A standard HWS mode was conducted in order to detect the onset temperature of a self-sustaining exothermal reaction ($T_{dT/dt>0.02°C/min}$), the onset temperature of a thermal runaway ($T_{dT/dt>0.2°C/min}$) and the temperature of the thermal runaway itself ($T_{dT/dt>10°C/min}$). All samples were heated stepwise from the starting temperature of 50°C to the limiting temperature of 350°C with a temperature increment of 5°C. After heating the sample by a 5°C step, the ARC switched from heating mode to wait mode for 30 min allowing for a temperature equalization at this temperature. Thereafter, the mode was changed to search mode, scanning for an exothermic reaction with a defined self-heating rate threshold of 0.02°C min^{-1}. In the consecutive exothermic mode, the vessel temperature of the ARC followed the sample temperature to simulate adiabatic test conditions. Overall, the temperature limit was set to 400°C if an exothermic reaction was detected. The sample temperature corresponding to a self-heating rate exceeding 0.2°C min^{-1} ($T_{dT/dt>0.2°C/min}$) was regarded to be the onset temperature of thermal runaway following the definition stated by Doughty et al.[4,39]

Results and Discussion

Within this section, the measurement data gained from ARC-HWS and XRD experiments on the electrode level is presented first, which is then discussed in terms of the underlying reaction kinetics by means of model based data analysis. These findings are compared to ARC-HWS experiments on the cell level. An overview of the carried out ARC-HWS experiments is given in Table I. The SoC and SoH range was chosen in accordance with the expected operating window of Li ion batteries, which is assumed to lie between 100% and 0% SoC as well as between 100% and 80% SoH.

Table I. ARC-HWS measurements carried out in this work.

		100% SoC	50% SoC	0% SoC
100% SoH	Anode	x	n/a*	n/a*
	Cathode	x	x	x
	Cell	x	x	x
80% SoH	Anode	x	n/a	n/a*
	Cathode	x	n/a	x
	Cell	x	n/a	n/a

x: measured.
n/a: not available as not measured.
n/a*: not available as no signal detected.

Electrode level tests.—Fig. 2 shows the results of ARC-HWS thermal stability investigations of harvested NMC-442 composite electrodes mixed with electrolyte at different SoC and SoH combinations. The higher the SoC, the lower the onset temperature of thermal runaway gets for both fresh and aged samples as shown in Figs. 2a and 2b. The impact of degree of lithiation on the onset temperature of thermal runaway for different grades of $LiNi_xCo_yMn_zO_2$ was shown previously, which supports the observations made here.[17] The sample at 100% SoC and 100% SoH showed an onset temperature of 179°C compared to 181°C and 187°C for 50% and 0% SoC. The measurements generally revealed a standard deviation of 1°C between two measurements and therefore, the observed difference in $T_{dT/dt>0.2°C/min}$ for 100% and 50% SoC is minor. The samples at 100% SoC and 80% SoH showed an onset temperature of 173°C compared to 178°C at 0% SoC. So, there is a considerable increase in onset temperature of thermal runaway of around 8°C and 5°C from the highest to the lowest SoC for the fresh and aged NMC-442 composite electrodes mixed with electrolyte. Similarly, the temperature rise of the first exothermic reaction (i.e. ΔT), represented by the width of the ARC-HWS plot in Fig. 2 increases with increasing SoC for both fresh and aged samples. This effect can be attributed to a decreasing structural stability of the active material during delithiation resulting not only in an increase in the total amount of heat release but also affecting the heat generation rate, which is resembled by the height of the ARC-HWS plot in Fig. 2.

Figs. 2c and 2d show ARC-HWS results of NMC-442 electrolyte mixtures depending on the SoH for both fully charged cells (i.e. 100% SoC, see Fig. 2c) and discharged cells (i.e. 0% SoC, see Fig. 2d). Both aged samples at 100% and 0% SoC showed a significant decrease in onset of thermal runaway from 179°C to 173°C and from 187°C to 178°C. This suggests that in the very beginning of an exothermic reaction, an aged cathode at an elevated degree of lithiation (i.e. 80% SoH and 0% SoC) shows a quite similar thermal behavior compared to a fresh cathode at a lower degree of lithiation (i.e. 100% SoH and 100% SoC). When further comparing the general shape of the ARC traces shown in Figs. 2c and 2d, the thermal stability seems to decrease with ongoing aging (i.e. a lower SoH) especially at higher degrees of lithiation (i.e. a lower SoC) confirming the observed trend of a decreasing onset temperature. Literature results from nail penetration experiments on commercially available full cells confirm the results showing that aging significantly decreases the time until a cell undergoes a thermal runaway.[11] The decreased thermal stability of the aged cathodes at lower levels of cell SoC can be explained by a lack of relithiation during aging caused e.g. by the growth of the cathode electrolyte interphase (CEI)[40] layer and/or by a contact loss of the cathode particles. The process of contact loss based on the formation of a CEI was shown previously.[41] The lacking relithiation during aging was confirmed via XRD measurements (see Fig. 3).[42] The (003) reflex is shifted to lower and the (101), (006) as well as the (102) reflexes are shifted to higher angles due to the expansion of the *c*-axis and the contractions of the *a*- and *b*-axis of the crystal structure during delithiation[43] (see Figs. 3a and 3b). The reflexes for the aged sample in the lithiated state corresponding to 0% cell SoC can be found at

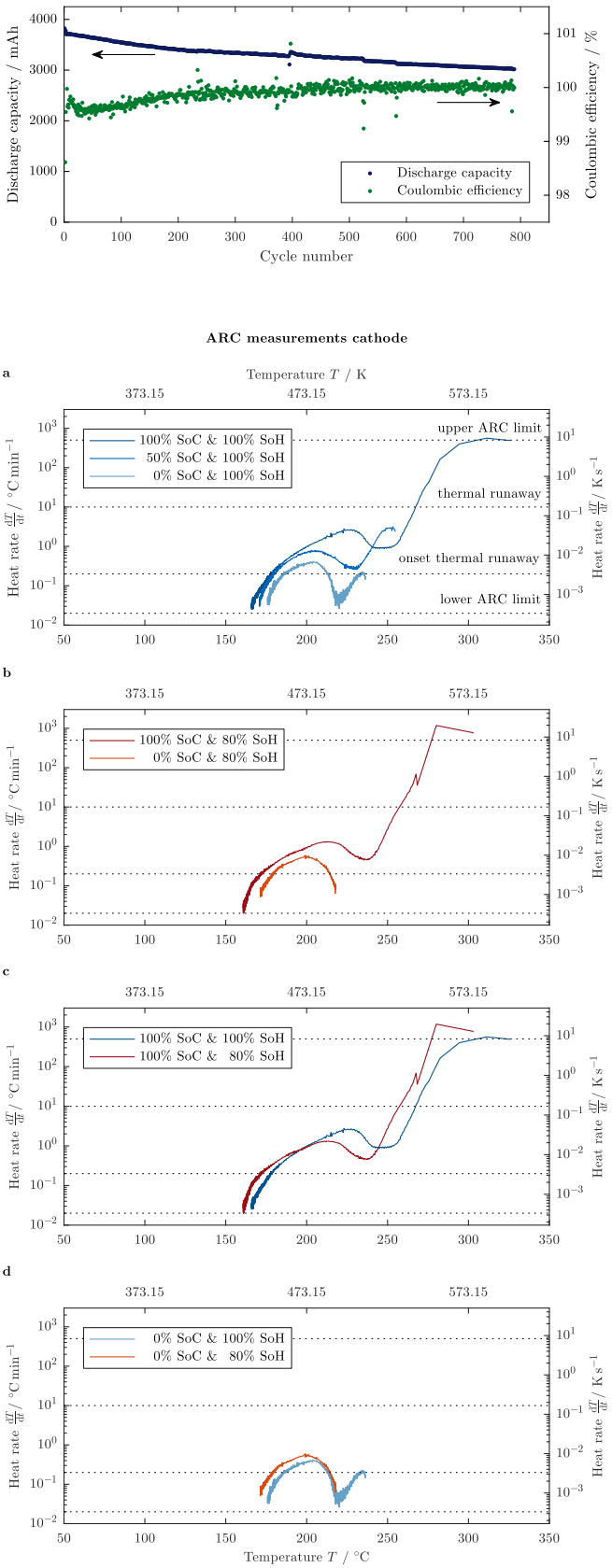

Figure 2. ARC-HWS results comparing the self-heating rate of NMC-442/electrolyte mixtures as a function of sample temperature indicating the SoC influence at 100% SoH (a), the SoC influence at 80% SoH (b), the impact of SoH at 100% SoC (c) and the impact of SoH at 0% SoC (d).

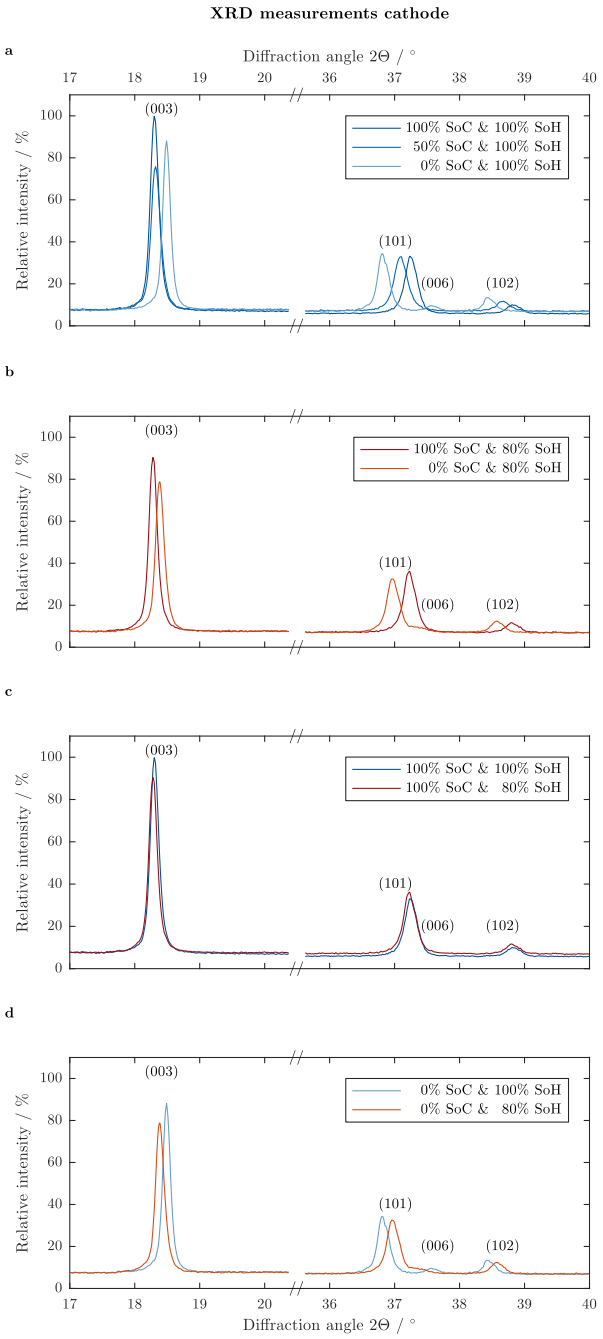

Figure 3. X-ray diffractograms of NMC-442/electrolyte mixtures indicating the SoC influence at 100% SoH (a), the SoC influence at 80% SoH (b), the impact of SoH at 100% SoC (c) and the impact of SoH at 0% SoC (d).

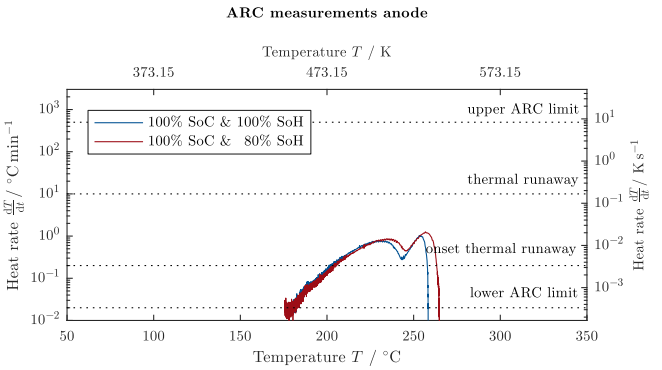

Figure 4. ARC-HWS results comparing the self-heating rate of MCMB/electrolyte mixtures as a function of sample temperature indicating the SoH influence at 100% SoC.

2Θ values in between the fresh samples at 0% and 100% SoC (see Fig. 3d) which indicates an incomplete relithiation during discharge. The comparably more delithiated structure remains less thermally stable and can therefore lead to a shift in $T_{dT/dt>0.2°C/min}$ to lower temperatures. In addition, the degree of lithiation for the samples at 100% SoC occurs to be similar for 80% and 100% SoH according to nearly equal 2Θ values observed in the X-ray diffractograms (see Fig. 3c).

Fig. 4 shows the ARC-HWS results of MCMB composite electrode/electrolyte mixtures. For anodes at 100% cell SoC, $T_{dT/dt>0.2°C/min}$ increases slightly from 100% to 80% SoH. Experiments on anodes at 50% and 0% SoC showed negligible exothermic reactions for both fresh and aged cells and are therefore not shown here. The values for the measured onset temperatures of thermal runaway on the electrode level are summarized in Table II.

It is also worth mentioning, that even with a comparably vast amount of composite electrode material (i.e. 0.55 g to 0.63 g) guaranteeing a thorough soaking with electrolyte (i.e. 0.63 g to 0.72 g), an exothermic decomposition reaction around 80°C to 120°C as previously reported[20] could not be observed in this work when testing the anode/electrolyte mixtures. On the cathode side, similar sample quantities were used for the composite electrode materials (i.e. 0.67 g to 0.76 g) and electrolyte (i.e. 0.74 g to 0.94 g). Also, it should be stated that the anode seems to be less reactive than the cathode within the whole temperature range from 160°C onwards for all SoC and SoH combinations never undergoing a runaway scenario which has been recently reported conversely for cells formed of artificial graphite and NMC-111.[44] Based on the electrode level measurements and the surprisingly not detectable decomposition and reformation reaction of the solid electrolyte interphase (SEI),[45] the authors cannot comment on any changes in the anode's reactivity below that temperature.

Electrode level reaction kinetics.—In order to quantify the observations made when comparing the ARC trace gathered during measurements, the underlying reaction kinetics are more closely investigated in this part. As already briefly discussed in the cathode section,

Table II. Temperature values for detected onset of thermal runaway on the electrode level $T_{dT/dt>0.2°C/min}$.

		100% SoC $T_{dT/dt>0.2°C/min}$ (°C)	50% SoC $T_{dT/dt>0.2°C/min}$ (°C)	0% SoC $T_{dT/dt>0.2°C/min}$ (°C)
100% SoH	Anode	202	-	-
	Cathode	179	181	187
80% SoH	Anode	203	-	-
	Cathode	173	-	178

The measured values exhibit a standard deviation of 1°C.

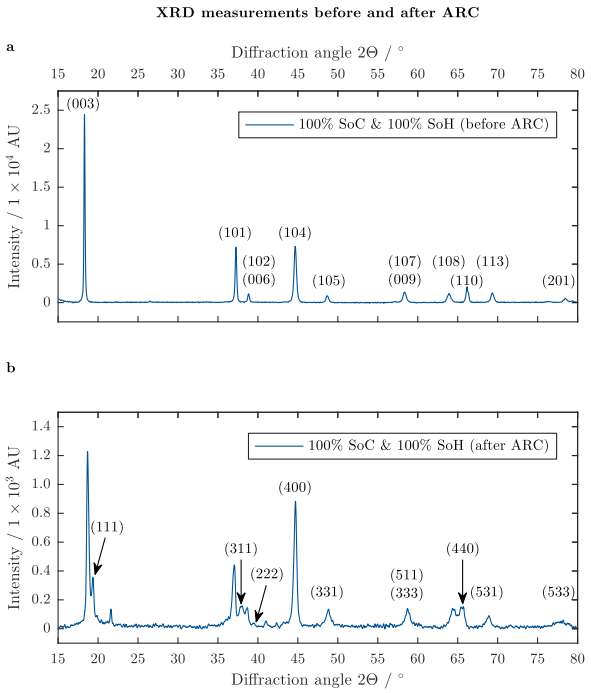

Figure 5. X-ray diffractograms of delithiated NMC-442 before (a) and after (b) ARC-HWS measurement up to 255°C.

ΔT can be assigned to the first exothermic reaction taking place involving a structural conversion from layered (space group $R\bar{3}m$) to cubic spinel phase (space group $Fd\bar{3}m$) via oxygen release and a subsequent combustion of the electrolyte.[46]

The transition to spinel phase was confirmed via XRD measurements which are shown in Fig. 5.[46–48] To obtain the presented powder diffractogram, the sample was heated to 255°C, stopping the ARC-HWS experiment to prevent further phase conversion. The (111) reflex is well visible and identifies besides other reflexes the formation of the spinel phase[46] (see Fig. 5b).

The highly reactive oxygen released during conversion can subsequently combust the flammable organic electrolyte via

$$C_3H_4O_3 + \frac{5}{2}O_2 \rightarrow 3CO_2 + 2H_2O \quad [1]$$

$$C_5H_{10}O_3 + 6O_2 \rightarrow 5CO_2 + 5H_2O \quad [2]$$

Previous works in the field have shown that ARC-HWS measurement data can be used to study reaction kinetics in order to obtain so called "kinetic triplets" including frequency factor γ (min^{-1}), activation energy E_a (eV) and reaction mechanism $f(\alpha)$ as a function of reaction conversion α.[20,32,33,49] These kinetic triplets can be used to simulate e.g. the underlying ARC-HWS trace or similar thermal stability tests. Due to the potential capability to predict the process of heat evolution during ARC-HWS measurements, deriving such kinetic triplets of the carried out two-component measurements as a function of both SoC and SoH is regarded to be of high importance for the community and this work.

The self-heating rate $\frac{dT}{dt}$ of a reaction follows Eq. 3.[33]

$$\frac{dT}{dt} = \frac{h}{C_{tot}} \cdot \frac{d\alpha}{dt} \quad [3]$$

With h as the total heat of the reaction (J), C_{tot} (J K^{-1}) as the total heat capacity of the sample and α as the degree of reaction conversion ($0 \leq \alpha \leq 1$). Hence, $\frac{d\alpha}{dt}$ represents the rate of reaction conversion depending on the rate constant k and the reaction model $f(\alpha)$ (see Table III).

$$\frac{d\alpha}{dt} = k \cdot f(\alpha) \quad [4]$$

Table III. Common reaction models and corresponding equations to describe the trace of the self-heating rate in ARC-HWS experiments.[50]

Reaction model (m-n-p)	$\frac{d\alpha}{dt} = \boldsymbol{k} \cdot \boldsymbol{f(\alpha)} = \boldsymbol{k} \cdot \boldsymbol{\alpha^m} \cdot (1-\boldsymbol{\alpha})^{\boldsymbol{n}} \cdot (-\ln(1-\boldsymbol{\alpha}))^{\boldsymbol{p}}$
0 order (0-0-0)	k
1st order (0-1-0)	$k \cdot (1-\alpha)$
2nd order (0-2-0)	$k \cdot (1-\alpha)^2$
Autocatalytic (1-1-0)	$k \cdot \alpha \cdot (1-\alpha)$
Avrami-Erofeev 1/2 (0-1-1/2)	$k \cdot (1-\alpha) \cdot (-\ln(1-\alpha))^{\frac{1}{2}}$
Avrami-Erofeev 2/3 (0-1-2/3)	$k \cdot (1-\alpha) \cdot (-\ln(1-\alpha))^{\frac{2}{3}}$
Avrami-Erofeev 3/4 (0-1-3/4)	$k \cdot (1-\alpha) \cdot (-\ln(1-\alpha))^{\frac{3}{4}}$

The rate constant k can be described via Eq. 5.

$$k = \gamma \cdot e^{-\frac{E_a}{k_B T}} \quad [5]$$

With γ as the frequency factor, E_a as the activation energy and the Boltzmann constant k_B.

$\frac{h}{C_{tot}}$ can be described as the total temperature increase for the reaction ΔT assuming a full conversion (i.e. $\alpha = 0 \ldots 1$) of the reaction (see Eq. 6).

$$\frac{h}{C_{tot}} = \Delta T \quad [6]$$

ΔT is mainly influenced by the so called phi-factor ϕ of the measurement.[22] It describes the ratio between material which takes part in the reaction (thermally active material) and material which only serves as a thermal mass (thermally inactive material) such as the calorimeter bomb or the current collector foils. It affects the temperature rise according to Eq. 7, whereas ΔT is the measured temperature rise as defined in Eq. 6. ϕ is defined in Eq. 8.

$$\Delta T_{ad} = \phi \cdot \Delta T \quad [7]$$

$$\phi = 1 + \frac{\sum \left(m_{inactive} \cdot c_{p,\ inactive}\right)}{\sum \left(m_{active} \cdot c_{p,\ active}\right)} \quad [8]$$

The estimated phi-factor values for the electrode level measurements ($\phi_{cathode} = 1.74$ and $\phi_{anode} = 1.90$) are higher but still comparable to the cell level measurements ($\phi_{cell} = 1.52$). The masses of each sample components and underlying heat capacities are summarized in Table IV. Combining Eq. 3 with Eq. 4, Eq. 5, and Eq. 6, the overall equation for the self-heating rate calculates as shown in Eq. 9

$$\frac{dT}{dt} = \Delta T \cdot \gamma \cdot e^{-\frac{E_a}{k_B T}} \cdot f(\alpha) \quad [9]$$

whereby γ, E_a and $f(\alpha)$ form the kinetic triplet which has to be determined to describe the reaction properly. Due to the nature of the equation and its number of variables, there are several solutions to fit ARC-HWS results.[20,32,33,57] To narrow down the choice of significant parameters to describe the function of self-heating rate vs. temperature, a linearization according to the reaction model was conducted. Self-heating rate curves were obtained which, in principle, are independent from any reaction model. By using this approach, the reaction mechanism can be eliminated from the equation, and γ as well as E_a can be then determined via the intersection with the y-axis and the slope of the linear part of the natural logarithm of the self-heating rate plotted against the reciprocal temperature (see Eq. 10).

$$\ln \frac{d\alpha}{dt} - \ln(f(\alpha)) = \ln \gamma - \frac{E_a}{k_B T} \quad [10]$$

Then, the linear part of the Arrhenius plot in Figs. 6b and 6d can be fitted for the cathode and anode side to obtain meaningful values for γ and E_a. As shown in Figs. 6a and 6c, the optimization procedure shows comparable results for both assumed reaction mechanisms even

Table IV. Sample masses studied in this work and corresponding heat capacities.

		Sample mass cell (g)	Sample mass anode (g)	Sample mass cathode (g)	Specific heat capacity c_p (J g^{-1} K^{-1})
Neg. current collector	Cu	14.42	0.27	-	0.385[a]
Neg. composite electrode	MCMB	31.27	0.55-0.63	-	0.800[b]
Separator	Polyester	8.69	-	-	2.480[c]
Pos. composite electrode	NMC-442	42.42	-	0.67-0.76	0.800[b,d]
Pos. current collector	Al	5.86	-	0.14	0.903[a]
Electrolyte	EC:DEC	27.60	0.63-0.72	0.74-0.94	2.055[a]
Pouch case	PA/Al/PP	5.65	-	-	1.212[e]
Ti vessel	Ti	-	2.97-3.05	2.98-3.04	0.523[f]
Steel holder	Fe	47.00	-	-	0.449[f]

[a]in accordance with.[51]
[b]approximated in accordance with.[52]
[c]in accordance with.[53]
[d]approximated in accordance with.[54]
[e]in accordance with.[55]
[f]in accordance with.[56]

though two similar but not identical sets of linear fits were derived from the linearization procedure (see Figs. 6b and 6d). The autocatalytic and Avrami-Erofeev type reaction mechanisms were chosen in the following as these were reported to show the most promising results for describing the decomposition of LCO/electrolyte mixtures[32,57] which could be confirmed for the studied NMC-442/electrolyte mixtures in this work. The exothermic reactions of the anode with the electrolyte involve the reaction of lithiated graphite with the conducting salt $LiPF_6$ and the solvent.[6,58,59] To allow for a most straightforward comparison between the electrodes, the same reaction mechanisms were chosen for the anode.

In order to find the most suitable set of γ and E_a for describing the ARC-HWS trace, an iterative least squares fit was carried out. First of all, the time equidistant data sets which were gathered every 30 s during the experiment were transformed to temperature equidistant data sets at temperature steps of 0.05°C via linear interpolation. This procedure is essential to not lay the focus of the fitting on measurement data gathered at the very early stages of thermal decomposition but to allow for a most thorough fit throughout the entire reaction. In the next step, the temperature ranges of both optimizing and linearizing needed to be defined. For both cathode and anode, the optimization range was chosen between the first detection of a self-sustaining decomposition reaction and the deflection point of the self-heating rate as a function of temperature (see Figs. 6a and 6c). The linearization range was reduced by 5 to 10°C from both the lower and upper end of the optimization range, approaching the peak heat generation rate at the top end of the linearization range (see Figs. 6b and 6d). This procedure showed most robust, reproducible and comparable results for all data sets based on the elimination of signal noise at lower temperatures and the exclusion of non-linear parts based on the applied reaction mechanism at elevated temperatures.

With a first guess for ΔT derived from the width of the ARC-HWS trace in Figs. 6a and 6c and assuming an almost negligible initial degree of conversion (i.e. $\alpha_0 \leq 1 \times 10^{-6}$) at the measured starting temperature T_0, a first linearization can be carried out. Based on this first linearization step and the derived values for γ and E_a, the ARC-HWS trace can be calculated numerically according to Eq. 9. In order to allow for an optimization, a cost function needs to be defined, which the authors chose as the sum of normalized squared errors (*SSE*) for both the predicted temperature and self-heating rate over all time steps in the optimization range

$$SSE = \sum_t \left(\left(1 - \frac{T_s}{T_m}\right)^2 + \left(1 - \frac{\frac{dT_s}{dt_s}}{\frac{dT_m}{dt_m}}\right)^2 \right) \quad [11]$$

whereas the subscript s and m denote simulated and measured values with $t_s \equiv t_m$. Together with the initial values as well as lower and upper limits for γ, E_a, ΔT, T_0 and α_0, these five values are iteratively varied to minimize the cost function *SSE*. The number of function evaluations and iterations is set to 1×10^5 and the absolute and relative tolerances are set to 1×10^{-9}. The lower and upper bounds for γ and E_a are derived from the standard deviation of the carried out linearization procedure which follows a standard linear least squares fit. The lower bound of ΔT is chosen as 0°C and the upper bound is the measured temperature increase for the entire ARC trace. The initial temperature of the reaction T_0 is chosen to lie between the minimum and maximum measured temperature and the corresponding initial degree of conversion α_0 is defined between 0 and 1. After this first optimization step, the whole procedure of linearizing and optimizing is repeated based on the calculated values for ΔT, T_0 and α_0. This results in a new set of γ and E_a, which is then the basis for the next optimization step. This procedure is repeated until a converged state can be observed after a maximum of 50 iterations. The convergence criterion is defined by the mean value of the derived coefficients of determination R^2_{tot} for the linearization procedure and the simulated values for the sample's temperature and self-heating rate.

$$R^2_{tot} = \frac{1}{3} \cdot \left(R^2_{lin} + R^2_T + R^2_{\frac{dT}{dt}} \right) \quad [12]$$

After R^2_{tot} does not alter more than 0.01% between two iterations, the solution corresponding to the maximum value of R^2_{tot} is chosen as the final solution of the linearization and optimization procedure. Exemplary values of R^2_{tot} for each measurement point are given in Table V for an Avrami-Erofeev 2/3 reaction model, which in sum showed the best performance in predicting the ARC-HWS trace of all studied reaction models for both electrodes.

The resulting simulated ARC-HWS traces for the studied Avrami-Erofeev 2/3 reaction model can be seen in Fig. 7 and Fig. 8 for the cathode and the anode side which were presented in analogy to Fig. 2 and Fig. 4. The results are also given in Table VI. It can be stated, that all derived fits show an excellent behavior for predicting the ARC-HWS trace with almost no visible deviation between the simulated and the measured values in the optimization range.

Except for the 0-order reaction, all reaction types summarized in Table III were used for the linearization and optimization procedure of all electrode samples presented in this work. First and second order reaction types are not shown due to their comparably poor performance in predicting the ARC-HWS trace for both electrodes. Generally, both autocatalytic and Avrami-Erofeev type reaction models showed similar R^2_{tot} values. Therefore, these reaction mechanisms are examined more closely in the following.

This procedure further allows for deriving the influence of SoC and SoH on kinetic parameters such as γ and E_a as presented in Fig. 9 and Table VI as well as the starting temperature T_{start} (i.e. $\alpha = 0$) and the specific heat of the reaction H (J g^{-1}) as shown in Fig. 10

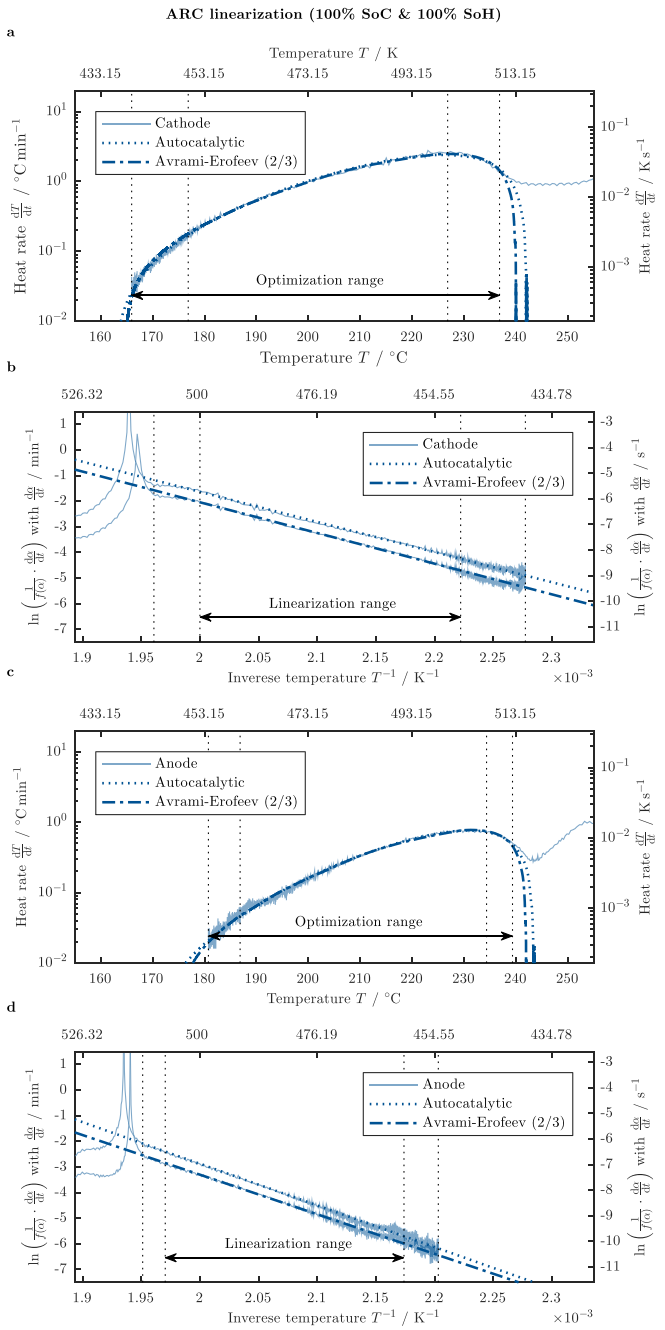

Figure 6. Linearization process of ARC-HWS measurements of NMC-442/electrolyte mixtures (a and b) and MCMB/electrolyte mixtures (c and d) at 100% SoC and 100% SoH applying two different reaction mechanisms.

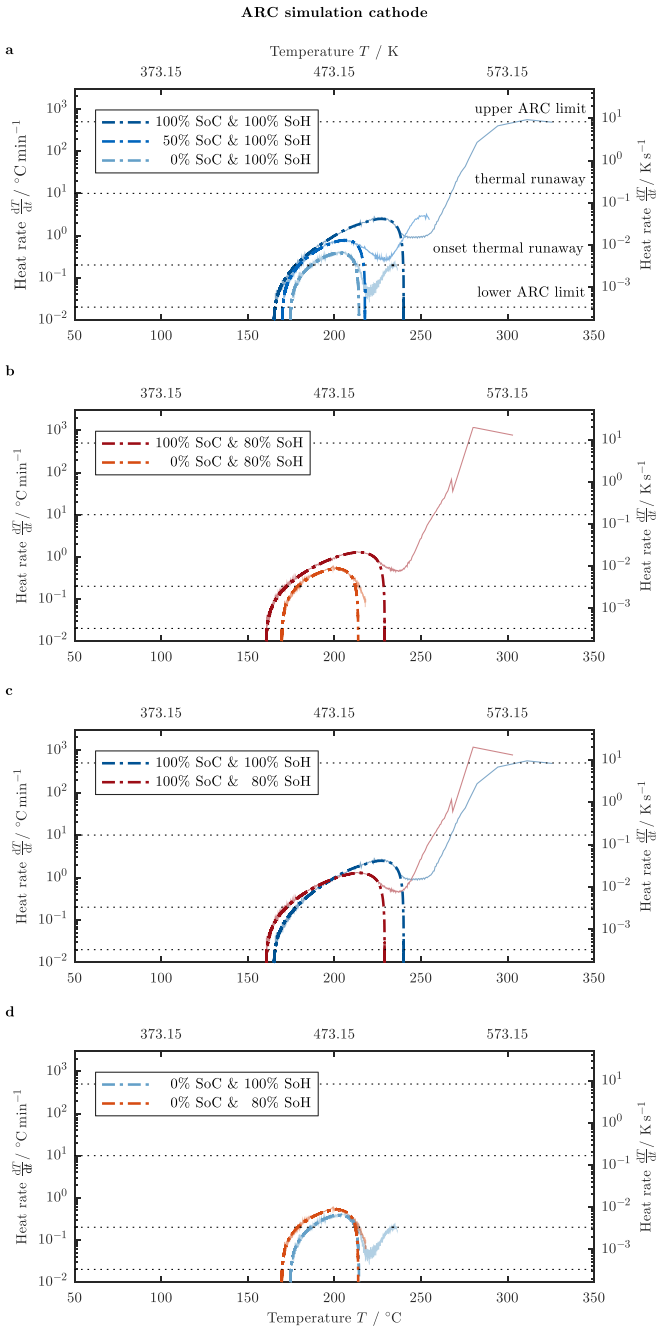

Figure 7. Simulated (Avrami-Erofeev 2/3, dash-dotted lines) and measured (solid lines) ARC-HWS results comparing the self-heating rate of NMC-442/electrolyte mixtures as a function of sample temperature indicating the SoC influence at 100% SoH (a), the SoC influence at 80% SoH (b), the impact of SoH at 100% SoC (c) and the impact of SoH at 0% SoC (d).

Table V. Mean values of the derived coefficients of determination R^2_{tot} for the linearization procedure and the simulated values for the sample's temperature and self-heating rate compared to measurement data (Avrami-Erofeev 2/3).

		100% SoC	50% SoC	0% SoC
100% SoH	Anode	99.65%	-	-
	Cathode	99.64%	99.27%	98.66%
80% SoH	Anode	99.69%	-	-
	Cathode	99.69%	-	98.53%

and Table VII with

$$H = \frac{h}{m_{\text{electrode}}} = \Delta T \cdot \frac{\sum_i m_i \cdot c_{p,i}}{m_{\text{electrode}}} \qquad [13]$$

whereas the indexes i accounts for all components of a sample as summarized in Table VI. All graphs are shown as a function of a decrease in capacity. As can be seen for all relevant reaction models, similar trends can be observed as long as the assumed reaction model is not altered for varying SoC and SoH combinations. The magnitude of the SoC and SoH influence varies slightly with the chosen reaction model as can be seen from the slopes and the absolute values in the

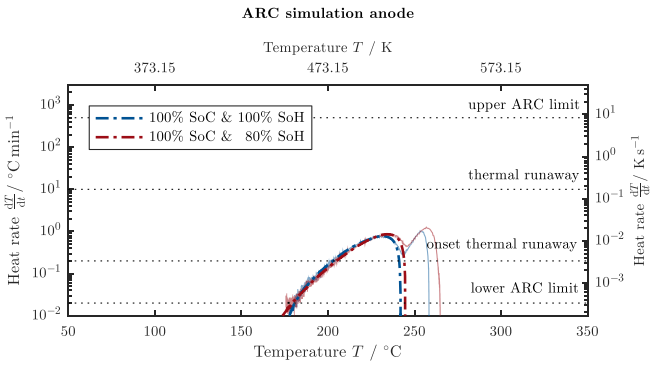

Figure 8. Simulated (Avrami-Erofeev 2/3, dash-dotted lines) and measured (solid lines) ARC-HWS results comparing the self-heating rate of MCMB/electrolyte mixtures as a function of sample temperature indicating the SoH influence at 100% SoC.

graphs. It can be also observed that both autocatalytic and Avrami-Erofeev type reaction models show similar results, which especially holds for the 2/3 and 3/4 shape on the cathode side and the 1/2 and 2/3 shape on the anode side.

At 100% SoH, the cathode reveals an exponential decrease of γ and a linear decrease of E_a with decreasing SoC (see Figs. 9a and 9b). At the same SoH, the cathode shows a linear increase of T_{start} and a quadratic decrease in H with decreasing SoC forming a minimum at 0% SoC (see Figs. 10a and 10b). For all remaining observations revealing the SoH influence, only trends can be described as only two data points are accessible in this work (i.e. 100% SoH and 80% SoH). On the cathode side, we can observe a strong decrease in both γ and E_a with decreasing SoH (see Figs. 9c and 9d). It is worth mentioning, that a cathode at 80% SoH with a low degree of lithiation (i.e. 100% cell SoC) shows similar values for γ and E_a as a cathode at 100% SoH at a high degree of lithiation (i.e. 0% cell SoC). With this observation alone, a simple influence of cell capacity or degree of lithiation on the thermal stability can be ruled out on the cathode side. As already observed from the ARC measurements, both the starting temperature of the reaction and the specific heat decrease with ongoing aging (see Figs. 10b and 10d). The anode in comparison reveals a contrary behavior in terms of γ and E_a compared to the cathode with ongoing aging. Both values increase with lower values in SoH (see Figs. 9e and 9f). Similar to the cathode, the starting temperature decreases for the anode, however, in a stronger manner (see Fig. 10e). Again contrary to the cathode, the specific heat increases with ongoing aging (see Fig. 10f).

When comparing the influence of SoC and SoH on each parameter, a straightforward tendency in terms of the overall reactivity cannot be stated without further considerations. From a reaction model perspective, a higher frequency factor combined with a lower activation energy would somewhat hint at a higher tendency to react whereas a lower frequency factor and a higher activation energy would indicate a lower tendency to react. This is not the case here as both frequency factor and activation energy either decrease or increase simultaneously. Together with the specific heat of the reaction, these factors represent the thermal stability of a sample over a wide range of temperatures (see Eq. 9). Therefore, they should be simultaneously evaluated to make a somewhat clearer statement.

For this purpose, the product of specific heat H and the reaction rate k are shown as a function of temperature for the cathode in Fig. 11 and for the anode in Fig. 12 highlighting the derived starting temperature of the reaction T_{start}. This product is further denoted as the specific reactivity of the sample (W g^{-1}). To further distinguish between the calculated values for varying SoC and SoH combinations, relative values are shown on the right side of both figures. From these figures, the influence of SoC and SoH becomes more apparent. On the cathode side, the reactivity is generally reduced at lower SoC levels for both fresh and aged cells, especially when considering the shift in T_{start} to higher values (Figs. 11b and 11d) resulting in an increased thermal stability with decreasing SoC. At temperatures below approximately 115°C, the reactivity for 0% SoC is slightly higher compared to 100% SoC but at this temperature, the reaction has not even started yet. With ongoing aging, the effect of SoC seems to be reduced which can be observed when comparing Figs. 11b to 11d. This becomes even more pronounced when comparing Figs. 11f to 11h. At 100% SoC, the cathode is more reactive at 80% SoH compared to 100% SoH at temperatures up to approximately 195°C but is less reactive afterwards. At 0% SoC, the aged cathode is more reactive throughout the entire duration of the first reaction (i.e. $<$ 220°C, as shown in Fig. 7d). Combined with the observed reduced T_{start}, aged cathodes are generally becoming more reactive than fresh cathodes at lower temperatures (see Fig. 11f). The temperature range, in which aged cathodes are more reactive than their fresh counterpart, also becomes larger at lower SoC values (Fig. 11h). This results in a comparably reduced thermal stability with ongoing aging especially at increasing degrees of lithiation.

Looking into the anode, the reactivity is reduced with ongoing aging at temperatures above approximately 175°C and below 230°C at 100% SoC (Figs. 12a and 12b). Beyond this temperature, the aged lithiated anode is more reactive than its fresh counterpart. Before the fresh anode starts to react at approximately 175°C, the aged anode is more reactive, as the reaction has already started at approximately 162°C. As no reaction could be detected at lower SoC values for both fresh and aged anodes, the SoC seems to be dominating the SoH influence in this case. It remains worth mentioning here, that for all SoC and SoH combinations, the cathode is more reactive than the anode for the temperature range, which we considered for fitting the presented reaction models (i.e. 150°C $<$ T $<$ 250°C) which agrees well with the observations made from comparing the ARC-HWS measurements shown in Fig. 2 and Fig. 4. Below this temperature range, the anode might be dominating based on the SEI-decomposition and reformation reaction, which will be discussed in the next section. Above that temperature range, a second, more reactive reaction seems to be dominating on the cathode side at lower degrees of lithiation (see Fig. 2c), which is by magnitudes larger than the small second reaction peak forming on the anode side (see Fig. 3b).

Cell level tests and simulations.—Results of ARC-HWS experiments on full cells with a nominal capacity of 5 Ah (i.e. $<$ 4 Ah at 4 C) consisting of MCMB as the anode and NMC-442 as the cathode are presented in Fig. 13 in order to show the influence of SoC and SoH on the full cell behavior. As already observed during the measurements on electrolyte wetted anodes and cathodes, the self-heating rate is highly dependent on the cell's SoC. The same can be seen in

Table VI. Values for frequency factor γ and activation energy of the reaction E_a derived from the optimization procedure (Avrami-Erofeev 2/3).

		100% SoC γ (s^{-1}) / E_a (J)	50% SoC γ (s^{-1}) / E_a (J)	0% SoC γ (s^{-1}) / E_a (J)
100% SoH	Anode	$1.66 \times 10^{+10}$ / 2.14×10^{-19}	-	-
	Cathode	$5.50 \times 10^{+07}$ / 1.65×10^{-19}	$7.12 \times 10^{+06}$ / 1.51×10^{-19}	$6.02 \times 10^{+05}$ / 1.38×10^{-19}
80% SoH	Anode	$6.08 \times 10^{+11}$ / 2.40×10^{-19}	-	-
	Cathode	$2.48 \times 10^{+05}$ / 1.30×10^{-19}	-	$3.23 \times 10^{+04}$ / 1.17×10^{-19}

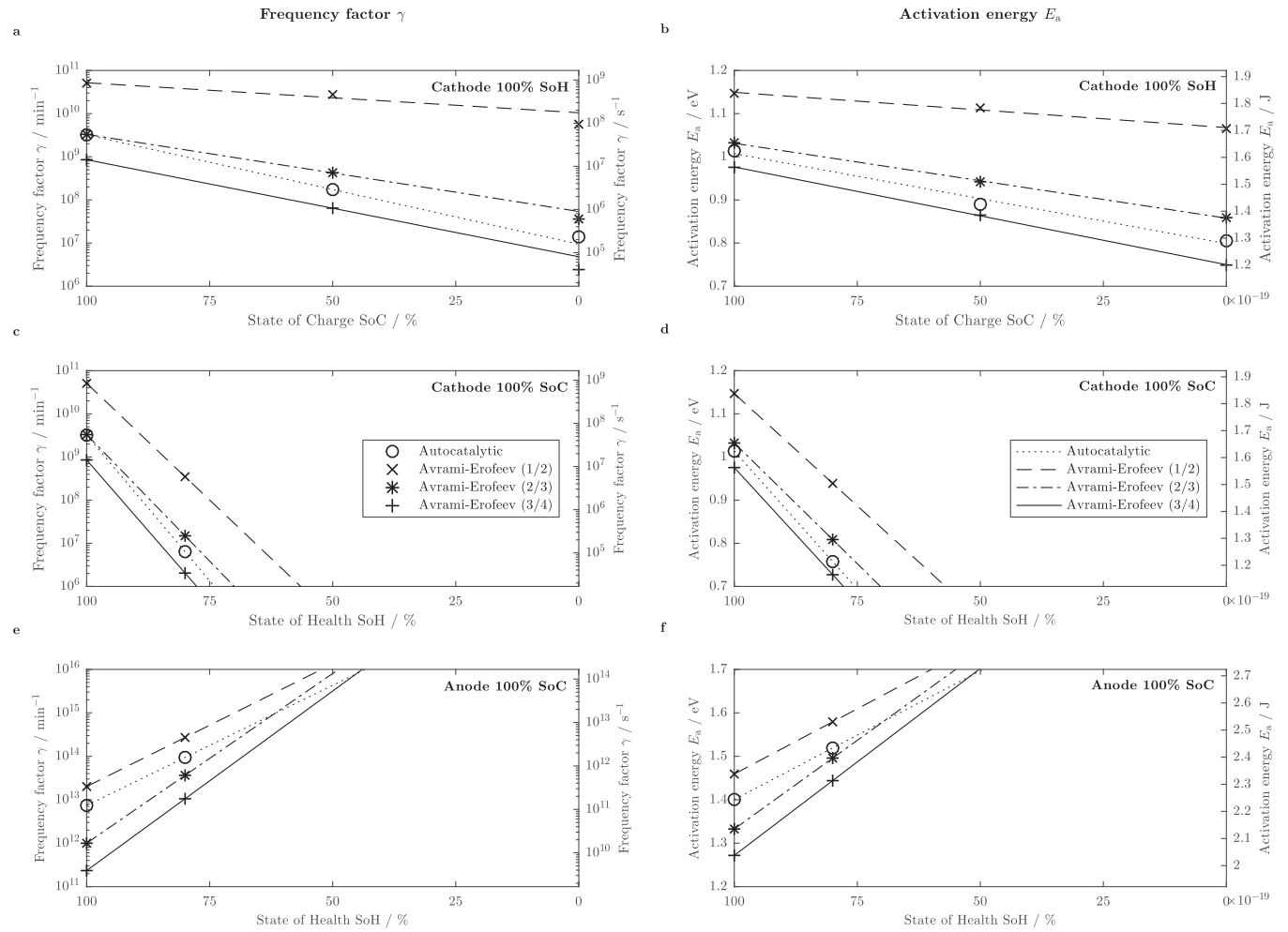

Figure 9. Frequency factor γ (left) and activation energy E_a (right) – influence of SoC (a and b) at 100% SoH as well as the influence of SoH (c and d) at 100% SoC on the cathode side and influence of SoH (e and f) at 100% SoC on the anode side for four different reaction models. Markers represent values summarized in Table VI and lines represent the underlying fit types shown in the Appendix.

Fig. 13a. In accordance with the two-component measurements, the reactivity increases with increasing SoC. Cells charged to 100% SoC undergo a thermal runaway whereas cells at 50% SoC just about border a runaway scenario and cells at 0% SoC do not cross the threshold of 10°C min^{-1} at all. This fits well to the two-component measurements performed on electrolyte wetted cathodes. Between 80°C and 135°C where the SEI is supposed to decompose and reform,[60] the self-heating rate is significantly lower for the cells which are not fully charged. The reason for the lower reactivity is probably based on the limited reformation of the SEI. After the SEI decomposes in fully charged cells, the SEI is directly reformed due to the low electrode potential and the high Li ion concentration at the surface of the active material particles.[6,20,61] Once the SEI is decomposed and the Li ion concentration in the anode is too low combined with a higher potential of the anode, the SEI can be only partially reformed. Generally, the heat release of the SEI decomposition is relatively small compared to what was observed in other studies.[21,62] The reactivity at temperatures from around 160°C onwards is similar to the two-component measurements on cathodes reported in this study (see Fig. 2) similarly showing a decrease in reactivity with decreasing SoC. Within this temperature range, the anode plays only a minor role in heat generation as already stated.

In order to investigate the influence of aging on the thermal stability of a full cell, ARC-HWS measurements were also carried out at 80% SoH (see Fig. 13b). Although the capacity of the whole cell is reduced by 20% at 4C, the reactivity seems to increase below temperatures of 160°C. This is well in line with the presented XRD results revealing the degree of lithiation within the cathode, which is not majorly affected by the SoH at 100% SoC (see Fig. 3c). Furthermore, ARC-HWS results in Fig. 2c and Fig. 12f show that the cathode reactivity is even increased at lower temperatures. In the case of a full cell, the self-heating rate from 160°C onwards is, however, not significantly influenced by aging. According to the here presented results, the reaction of the cathode with the electrolyte is expected to dominate within that temperature range. Only the temperature range before 160°C reveals a stronger reactivity for the aged cell. In this area, the anode (i.e. lithium within the anode) is supposed to react with the electrolyte.[6] As already mentioned, ARC-HWS results on fully charged anodes presented in this work do not show any exothermic reactions at such an early stage. On the one hand, this may be attributed to the comparably lower active material share and the consequently higher ϕ-factor during the two-component measurement. On the other hand, the electrode composition could have changed after cell opening; oxygen from the air in the dry room could have reacted with the lithium in the anode and possible decomposition products could have evaporated. Studying these effects should be within the scope of further work. If, however, these assumptions hold true, measurements on the cell level are very important to gain in-situ information about the processes occurring during thermal abuse. For a distinct analysis of each material's reactivity in a full cell, the measurement is, however, not sensitive enough due to simultaneously occurring reactions, which are difficult to separate in the overall

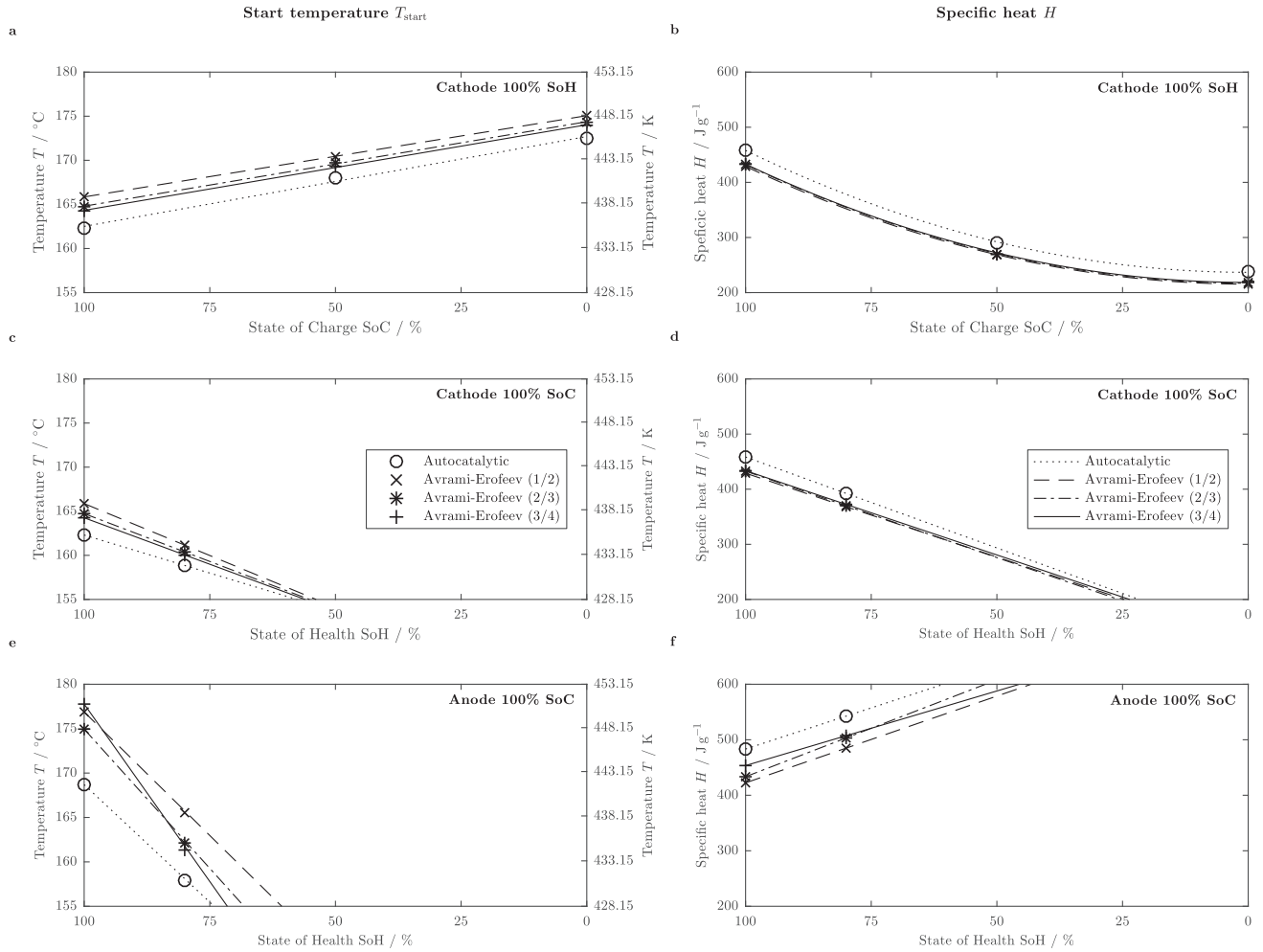

Figure 10. Start temperature T_{start} (left) and specific heat H (right) – influence of SoC (a and b) at 100% SoH as well as the influence of SoH (c and d) at 100% SoC on the cathode side and influence of SoH (e and f) at 100% SoC on the anode side for four different reaction models. Markers represent values summarized in Table VII and lines represent the underlying linear fits for T_{start} and the fit types shown in the Appendix for H.

ARC-HWS trace. Therefore, it depends on the scope of a study which level should be preferably investigated. In this work, both electrode and cell level are considered to draw a more complete picture of cell thermal stability.

In order to describe the full cell behavior based on the identified two-component reaction kinetics, their individual impact on the temperature evolution needs to be considered via

$$\frac{dT}{dt} = \frac{1}{C_{p,\,\mathrm{cell}}} \sum_i \left(m_i \cdot H_i \cdot e^{-\frac{E_{a,i}}{k_B T}} \cdot (1-\alpha_i) \cdot (-\ln(1-\alpha_i))^{\frac{2}{3}} \right) \quad [14]$$

whereas the indexes i denotes the decomposition reaction on the anode or cathode side weighed with the respective composite electrode mass m_i and degree of reaction conversion α_i, which is calculated individually according to Eq. 4 and Eq. 5.

The kinetic description of the full cell behavior based on the two-component measurements appeared to be challenging as can be seen in Fig. 14. Exothermic reactions involving several reaction partners from both anode and cathode take place at the same time, which seems to be difficult to depict via two-component measurements alone. Furthermore, the two-component measurements did not show any exothermic reactions below 160°C so that the kinetics could not be determined for this temperature range. That makes a complete description impossible based on the here presented results. For this temperature range, the reader is referred to previous publications which form the basis for this work.[20,30] Basically, five different events can be identified when comparing the simulated cell behavior to the measured cell

Table VII. Values for start temperature T_{start} (i.e. $\alpha = 0$) and specific heat of the reaction H (i.e. $\alpha = 0 \ldots 1$) derived from the optimization procedure (Avrami-Erofeev 2/3).

		100% SoC T_{start} (°C) / H (J g^{-1})	50% SoC T_{start} (°C) / H (J g^{-1})	0% SoC T_{start} (°C) / H (J g^{-1})
100% SoH	Anode	174.95 / 433.40	-	-
	Cathode	165.95 / 432.74	170.82 / 269.14	175.82 / 218.33
80% SoH	Anode	162.13 / 503.22	-	-
	Cathode	161.03 / 370.02	-	171.30 / 258.20

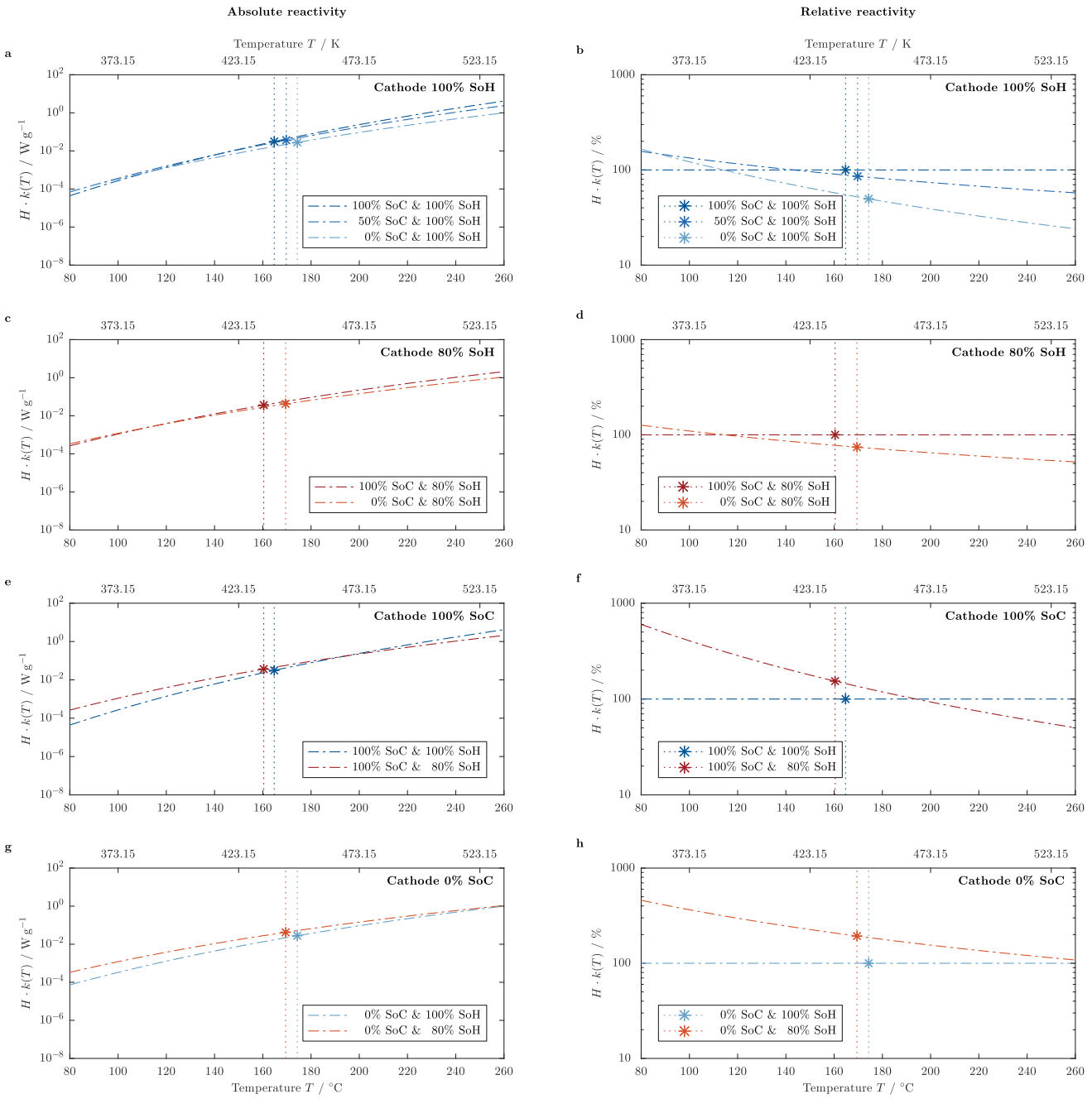

Figure 11. Results from the linearization and optimization procedure (Avrami-Erofeev 2/3) comparing the reactivity of NMC-442/electrolyte mixtures as a function of sample temperature (dash-dotted lines, T_{start} marked with asterisks and vertical lines) indicating the SoC influence at 100% SoH (a and b), the SoC influence at 80% SoH (c and d), the impact of SoH at 100% SoC (e and f) and the impact of SoH at 0% SoC (g and h).

behavior at 100% SoC. From ∼80°C to ∼135°C, the SEI is supposed to decompose (1) and subsequently it is reformed (2) from ∼135°C to ∼160°C.[20] From ∼160°C onwards, the cathode starts to decompose and react with the electrolyte (3) as we showed in our study. Between ∼215°C and ∼235°C, the polyester based separator is expected to melt consuming heat during the melting process leading to consecutive short circuits in the cell (4). This temperature span falls in the range of the melting point of polyesters. According to the manufacturer, the heat resistivity of the separator lies around 270°C due to its ceramic coating, which could even prevent the formation of severe internal short circuits up to this temperature. Above ∼235°C the cathode is expected to release further oxygen accelerating the reaction with the electrolyte (5) as also shown in Fig. 2c. The reaction of the anode with the electrolyte seems to play only a minor role within that temperature range, and is expected to significantly contribute to the self-heating of the cell at temperatures from ∼250°C onwards based on the lower reactivity compared to the cathode as discussed in the previous section and shown by the simulated second peak shown in Fig. 14. As a result of the combination of events and the varying dominance of reactions, each reaction's impact on the ARC trace may be shifted to higher temperatures in comparison to the two-component measurements as can be observed when looking into the impact of the anode on the simulated cell behavior.

In general, the self-heating rate during the full cell measurement is higher compared to the two-component measurements. On the one hand, this can be attributed to the already mentioned combination

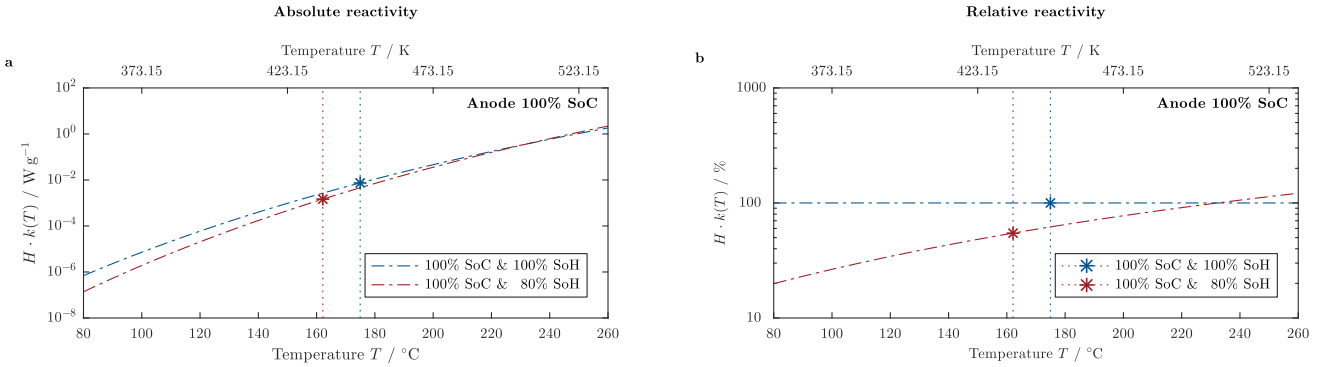

Figure 12. Results from the linearization and optimization procedure (Avrami-Erofeev 2/3) comparing the self-heat rate of MCMB/electrolyte mixtures as a function of sample temperature (dash-dotted lines, T_{start} marked with asterisks and vertical lines) indicating the SoH influence at 100% SoC.

and interaction of reactions within the full cell. On the other hand, the slightly larger share of thermally active mass in the pouch cell ($\phi_{cell} = 1.52$) leads to a higher self-heating rate compared to the two-component measurements ($\phi_{cathode} = 1.74$ and $\phi_{anode} = 1.90$), according to Eq. 7 and Table IV. Furthermore, a leakage or a rupture of the pouch foil resulting from a gassing of the electrolyte (evaporation of DEC starting at ∼127°C[63]) could have led to a contact between the electrolyte wetted electrode materials with environmental oxygen which could significantly increase the overall intensity of the reaction. At a temperature of ∼162°C, an abrupt voltage drop to 0 V could be observed which might hint at a severe electrolyte leakage or even the formation of a hard internal short involving excessive heating. In the two-component measurements carried out in this work, a contamination of the electrolyte wetted electrode materials with environmental oxygen was not possible due to the applied gastight Ti vessels. Based on the two-component systems investigated, also short circuits were not possible to form.

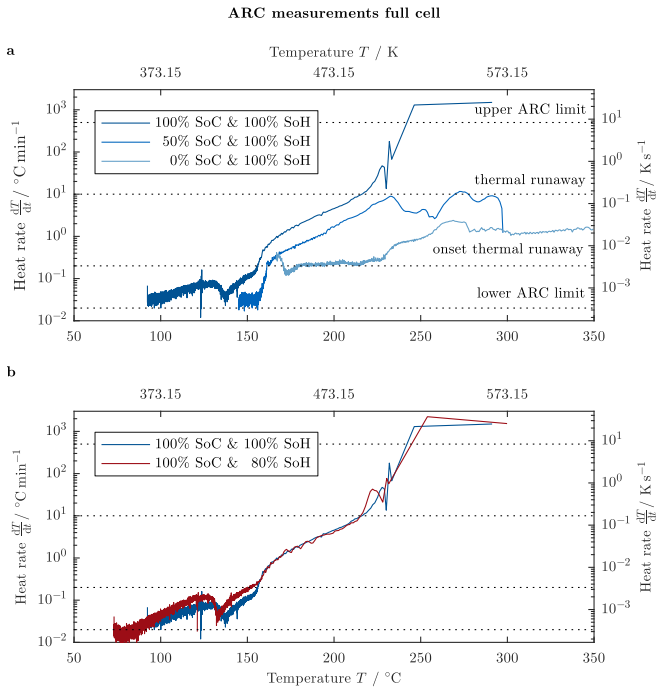

Figure 13. ARC-HWS results comparing the self-heating rate of 5 Ah pouch cells with MCMB as the anode and NMC-442 as the cathode as a function of sample temperature indicating the SoC influence at 100% SoH (a) and the impact of SoH at 100% SoC (b).

Conclusions

Within this work, a comprehensive thermal study on 5 Ah pouch cells (NMC-442/MCMB) and its thermally active components was presented based on combined ARC-HWS and XRD measurements. Composite anode and cathode materials were harvested from the studied 5 Ah pouch cells at defined states (i.e. 100%, 50%, and 0% cell SoC & 100% and 80% cell SoH) which were mixed with the used electrolyte (1 M $LiPF_6$ in EC:DEC 3:7 (by weight) + 2 wt% VC + 0.5 wt% LiBOB) and placed in gastight Ti vessels. The studied cathode samples showed an increase in the onset temperature of thermal runaway between 8°C and 5°C with decreasing SoC from 100% to 0% SoC for fresh and aged samples. Aging from 100% to 80% SoH led a decrease in onset temperature of thermal runaway up to 6°C for more delithiated cathodes (i.e. 100% cell SoC) and up to 9°C for more lithiated cathodes (i.e. 0% cell SoC). XRD measurements revealed that aged cathodes showed a lower degree of lithiation at 0% SoC which explains the higher reactivity in mixture with electrolyte with ongoing aging especially at a low cell SoC. The studied anode samples showed a comparably lower self-heating rate for all SoC and SoH combinations. For SoC values lower than 100%, no self-sustaining exothermic reaction could be detected at all. At 100% SoC, a negligible increase in onset temperature of thermal runaway could be observed with ongoing aging.

Avrami-Erofeev and autocatalytic reaction models were considered to describe the ARC trace of the two-component measurements, which allowed for a comparison of kinetic parameters such as the activation energy as well as the frequency factor of each reaction. For this purpose, a linearization of the ARC trace was performed based on the assumed reaction model, which was fitted in an iterative least squares

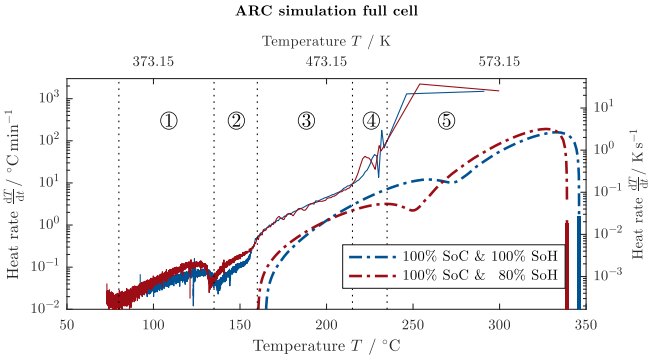

Figure 14. Simulated (Avrami-Erofeev 2/3, dash-dotted lines) and measured (solid lines) ARC-HWS results comparing the self-heating rate of 5 Ah pouch cells with MCMB as the anode and NMC-442 as the cathode as a function of sample temperature indicating the SoH influence at 100% SoC.

manner to the measurement data. It could be shown, that considering these parameters on their own did not necessarily lead to a straightforward conclusion in terms of relative changes in the reactivity of a sample as both activation energy and frequency factor simultaneously increased or decreased but never changed in opposing directions which would have been much easier to interpret. The authors showed that by evaluating the reaction rate constant together with the specific heat and the starting temperature of the reaction, the tendency observed during the ARC-HWS measurements could be analytically explained. With this approach, the qualitatively observed increase in reactivity of the cathode with ongoing aging at reduced SoC levels could be quantitatively confirmed. As the cathode was dominating in terms of the overall reactivity in this case, this implied a larger safety threat for cyclic aged cells compared to fresh cells, which especially holds for lower SoC values.

In accordance with the two-component measurements, full cells also showed a comparably lower reactivity with decreasing SoC and a relatively higher reactivity with ongoing aging. However, the first exothermic reactions occur at much lower temperatures compared to the two-component measurements, which may be attributed to the decomposition and reformation reaction of the SEI. This reaction could not be observed during the two-component measurements of the corresponding anode, which the authors believe to be primarily based on the chosen sample preparation in a dry room environment and the comparably higher ϕ-factor of the two-component measurements itself. Based on the identified reaction models from the two-component measurements, the full cell ARC trace could be simulated. However, the predicted ARC trace did not fully resemble the tendencies observed during the full cell measurements. On the one hand, this could be attributed to the already mentioned lacking description of the SEI decomposition and reformation reaction as well as the lacking description of further processes such as separator melting or cell shorting in this study. On the other hand, possible cross-interactions between reaction species from the anode and the cathode could not be depicted via two-component measurements alone. What is more, a possible rupture of the pouch seam during the full cell measurement might resulted in a contamination of the reaction with environmental oxygen. Further research will be conducted regarding the active mass ratio of the two-component measurements to increase the detectable signal and considering the sample preparation to avoid the evaporation of volatile components as can be found e.g. in the SEI. Based on the depicted reaction models, the thermal stability of NMC-442/MCMB cells can be described during various abuse scenarios as both a function of SoC and SoH, which will be of particular interest for modeling and simulation purposes of this cell chemistry.

Acknowledgment

The work presented here was supported by the German Federal Ministry of Education and Research (03X4631N and 03X4631P, *SafeBatt*). The authors thank Oliver Nolte from Volkswagen AG and Juhyon Lee from BMW AG for supporting the work with fruitful discussions.

Appendix

In order to be able to describe the underlying reaction kinetics of a cell individually as a function of SoC (0. . . 1) and SoH (0.8. . . 1), relevant kinetic parameters (see Table VI and Table VII) such as the frequency factor γ (s^{-1}), the activation energy E_a (J) and the specific heat of the reaction H (J g^{-1}) were fitted according to an Avrami-Erofeev 2/3 reaction model. For the cathode side, Eq. A1, Eq. A2 and Eq. A3 apply.

$$\gamma_{ca}\,(SoC,\,SoH) = 0.0535 \cdot e^{(-6.2607 \cdot SoC + 10.3735 \cdot SoC \cdot SoH + 16.6386 \cdot SoH)} \quad [A1]$$

$$E_{a,ca}(SoC,\,SoH) = ((0.7487 \cdot SoH - 0.4707) \cdot SoC + (1.0341 \cdot SoH + 0.3400)) \cdot 1 \times 10^{-19} \quad [A2]$$

$$H_{ca}(SoC,\,SoH) = (517.2133 \cdot SoH - 301.9439) \cdot SoC^2 + (-205.7713 \cdot SoH + 422.8129) \quad [A3]$$

As no self-sustaining exothermal decomposition reaction could be detected for SoC values of 50% and 0%, reaction kinetics on the anode side can be only described as a function of SoH (0.8. . . 1) at 100% SoC.

$$\gamma_{an}\,(SoH) = 1.0849 \times 10^{18} \cdot e^{-17.9926 \cdot SoH} \quad [A4]$$

$$E_{a,an}\,(SoH) = (-1.3077 \cdot SoH + 3.4429) \cdot 1 \times 10^{-19} \quad [A5]$$

$$H_{an}\,(SoH) = -349.1208 \cdot SoH + 782.5197 \quad [A6]$$

ORCID

A. Rheinfeld https://orcid.org/0000-0003-0995-7266

References

1. P. Meister, H. Jia, J. Li, R. Kloepsch, M. Winter, and T. Placke, *Chem. Mater.*, **28**(20), 7203 (2016).
2. T. Placke, R. Kloepsch, S. Dühnen, and M. Winter, *J Solid State Electrochem*, **21**(7), 1939 (2017).
3. R. Wagner, N. Preschitschek, S. Passerini, J. Leker, and M. Winter, *J. Appl. Electrochem.*, **43**(5), 481 (2013).
4. D. H. Doughty and E. P. Roth, *Electrochem. Soc. Interface*, **21**(2), 37 (2012).
5. P. G. Balakrishnan, R. Ramesh, and T. Prem Kumar, *J. Power Sources*, **155**(2), 401 (2006).
6. P. Biensan, B. Simon, J. P. Pérès, A. de Guibert, M. Broussely, J. M. Bodet, and F. Perton, *J. Power Sources*, **81–82**(0), 906 (1999).
7. M. Börner, A. Friesen, M. Grützke, Y. P. Stenzel, G. Brunklaus, J. Haetge, S. Nowak, F. M. Schappacher, and M. Winter, *J. Power Sources*, **342**, 382 (2017).
8. E. P. Roth and D. H. Doughty, *J. Power Sources*, **128**(2), 308 (2004).
9. P. Röder, B. Stiaszny, J. C. Ziegler, N. Baba, P. Lagaly, and H.-D. Wiemhöfer, *J. Power Sources*, **268**, 315 (2014).
10. M. Fleischhammer, T. Waldmann, G. Bisle, B.-I. Hogg, and M. Wohlfahrt-Mehrens, *J. Power Sources*, **274**, 432 (2015).
11. S. Hildebrand, A. Friesen, J. Haetge, V. Meier, F. Schappacher, and M. Winter, *ECS Trans.*, **74**(1), 85 (2016).
12. J. Vetter, P. Novák, M. R. Wagner, C. Veit, K.-C. Möller, J. O. Besenhard, M. Winter, M. Wohlfahrt-Mehrens, C. Vogler, and A. Hammouche, *J. Power Sources*, **147**(1–2), 269 (2005).
13. M. Reichert, J. Haetge, D. Berghus, C. Wendt, V. Meier, U. Rodehorst, S. Passerini, F. Schappacher, and M. Winter, *ECS Trans.*, **61**(27), 87 (2014).
14. J. Jiang and J. R. Dahn, *Electrochem. Commun.*, **6**(1), 39 (2004).
15. Y. Wang, J. Jiang, and J. R. Dahn, *Electrochem. Commun.*, **9**(10), 2534 (2007).
16. S. Hildebrand, C. Vollmer, M. Winter, and F. M. Schappacher, *J. Electrochem. Soc.*, **164**(9), A2190 (2017).
17. L. Ma, M. Nie, J. Xia, and J. R. Dahn, *J. Power Sources*, **327**, 145 (2016).
18. S. Brox, S. Roser, T. Husch, S. Hildebrand, O. Fromm, M. Korth, M. Winter, and I. Cekic-Laskovic, *ChemSusChem*, **9**(13), 1704 (2016).
19. S. Brox, S. Röser, B. Streipert, S. Hildebrand, U. Rodehorst, X. Qi, R. Wagner, M. Winter, and I. Cekic-Laskovic, *ChemElectroChem*, **4**(2), 304 (2017).
20. M. N. Richard and J. R. Dahn, *J. Electrochem. Soc.*, **146**(6), 2068 (1999).
21. A. Friesen, F. Horsthemke, X. Mönnighoff, G. Brunklaus, R. Krafft, M. Börner, T. Risthaus, M. Winter, and F. M. Schappacher, *J. Power Sources*, **334**, 1 (2016).
22. D. I. Townsend and J. C. Tou, *Thermochim. Acta*, **37**(1), 1 (1980).
23. X. Feng, J. Sun, M. Ouyang, F. Wang, X. He, L. Lu, and H. Peng, *J. Power Sources*, **275**, 261 (2015).
24. J. Geder, H. E. Hoster, A. Jossen, J. Garche, and D. Y. Yu, *J. Power Sources*, **257**, 286 (2014).
25. S. EL Khakani, D. Rochefort, and D. D. MacNeil, *J. Electrochem. Soc.*, **163**(7), A1311 (2016).
26. G.-Y. Kim and J. R. Dahn, *J. Electrochem. Soc.*, **160**(8), A1108 (2013).
27. R. Spotnitz and J. Franklin, *J. Power Sources*, **113**(1), 81 (2003).
28. T. D. Hatchard, D. D. MacNeil, A. Basu, and J. R. Dahn, *J. Electrochem. Soc.*, **148**(7), A755 (2001).
29. S. U. Kim, P. Albertus, D. Cook, C. W. Monroe, and J. Christensen, *J. Power Sources*, **268**, 625 (2014).
30. M. N. Richard and J. R. Dahn, *J. Electrochem. Soc.*, **146**(6), 2078 (1999).
31. D. D. MacNeil, T. D. Hatchard, and J. R. Dahn, *J. Electrochem. Soc.*, **148**(7), A663 (2001).
32. D. D. MacNeil, L. Christensen, J. Landucci, J. M. Paulsen, and J. R. Dahn, *J. Electrochem. Soc.*, **147**(3), 970 (2000).
33. D. D. MacNeil and J. R. Dahn, *J. Phys. Chem. A*, **105**(18), 4430 (2001).
34. P. Peng, Y. Sun, and F. Jiang, *Heat Mass Transfer*, **50**(10), 1405 (2014).
35. P. T. Coman, E. C. Darcy, C. T. Veje, and R. E. White, *J. Electrochem. Soc.*, **164**(4), A587 (2017).
36. G.-H. Kim, A. Pesaran, and R. Spotnitz, *J. Power Sources*, **170**(2), 476 (2007).
37. C. von Lüders, V. Zinth, S. V. Erhard, P. J. Osswald, M. Hofmann, R. Gilles, and A. Jossen, *J. Power Sources*, **342**, 17 (2017).
38. V. Zinth, C. von Lüders, M. Hofmann, J. Hattendorff, I. Buchberger, S. Erhard, J. Rebelo-Kornmeier, A. Jossen, and R. Gilles, *J. Power Sources*, **271**, 152 (2014).

39. D. H. Doughty, *Vehicle Battery Safety Roadmap Guidance*, (2012).
40. R. Wagner, B. Streipert, V. Kraft, A. Reyes Jiménez, S. Röser, J. Kasnatscheew, D. R. Gallus, M. Börner, C. Mayer, H. F. Arlinghaus, M. Korth, M. Amereller, I. Cekic-Laskovic, and M. Winter, *Adv. Mater. Interfaces*, **3**(15), 1600096 (2016).
41. Y. Qian, P. Niehoff, M. Börner, M. Grützke, X. Mönnighoff, P. Behrends, S. Nowak, M. Winter, and F. M. Schappacher, *J. Power Sources*, **329**, 31 (2016).
42. B. J. Hwang, Y. W. Tsai, D. Carlier, and G. Ceder, *Chem. Mater.*, **15**(19), 3676 (2003).
43. M. Balasubramanian, X. Sun, X. Yang, and J. McBreen, *J. Power Sources*, **92**(1-2), 1 (2001).
44. T. Inoue and K. Mukai, *Electrochem. Commun.*, **77**, 28 (2017).
45. M. Winter, *Z. Phys. Chem.*, **223**(10-11), 1395 (2009).
46. S.-M. Bak, E. Hu, Y. Zhou, X. Yu, S. D. Senanayake, S.-J. Cho, K.-B. Kim, K. Y. Chung, X.-Q. Yang, and K.-W. Nam, *ACS Appl. Mater. Interfaces*, **6**(24), 22594 (2014).
47. H. Wang, Y.-I. Jang, B. Huang, D. R. Sadoway, and Y.-M. Chiang, *J. Electrochem. Soc.*, **146**(2), 473 (1999).
48. S.-T. Myung, K.-S. Lee, C. S. Yoon, Y.-K. Sun, K. Amine, and H. Yashiro, *J. Phys. Chem. C*, **114**(10), 4710 (2010).
49. D. D. MacNeil and J. R. Dahn, *J. Electrochem. Soc.*, **148**(11), A1205 (2001).
50. M. E. Brown, D. Dollimore, A. K. Galwey, C. H. Bamford, C. F. H. Tipper, and Editors, *Reactions in the solid state*, New York, Amsterdam, New York, Elsevier Scientific Pub. Co (1980).
51. S. C. Chen, C. C. Wan, and Y. Y. Wang, *J. Power Sources*, **140**(1), 111 (2005).
52. A. Loges, S. Herberger, P. Seegert, and T. Wetzel, *J. Power Sources*, **336**, 341 (2016).
53. V. Vishwakarma and A. Jain, *J. Power Sources*, **272**, 378 (2014).
54. P. Gotcu and H. J. Seifert, *PCCP*, **18**(15), 10550 (2016).
55. A. Rheinfeld, S. Kosch, S. V. Erhard, P. J. Osswald, B. Rieger, and A. Jossen, *J. Electrochem. Soc.*, **163**(14), A3046 (2016).
56. David R. Lide, Editor, *CRC Handbook of Chemistry and Physics: 84th Edition*, CRC Press (2003).
57. D. D. MacNeil and J. R. Dahn, *J. Electrochem. Soc.*, **149**(7), A912 (2002).
58. T. Inoue and K. Mukai, *ACS Appl. Mater. Interfaces*, **9**(2), 1507 (2017).
59. J. Yamaki, H. Takatsuji, T. Kawamura, and M. Egashira, *Solid State Ion.*, **148**(3-4), 241 (2002).
60. H. H. Lee, C. C. Wan, and Y. Y. Wang, *J. Electrochem. Soc.*, **151**(4), A542 (2004).
61. H. Park, T. Yoon, Y. Kim, J. G. Lee, J. Kim, H.-s. Kim, J. H. Ryu, J. J. Kim, and S. M. Oh, *J. Electrochem. Soc.*, **162**(6), A892 (2015).
62. Z. Zhang, D. Fouchard, and J. R. Rea, *J. Power Sources*, **70**(1), 16 (1998).
63. D. Li, W. Fang, Y. Xing, Y. Guo, and R. Lin, *J. Hazard. Mater.*, **161**(2-3), 1193 (2009).

Erratum: Thermal Analysis of $LiNi_{0.4}Co_{0.2}Mn_{0.4}O_2$/Mesocarbon Microbeads Cells and Electrodes: State-of-Charge and State-of-Health Influences on Reaction Kinetics [*J. Electrochem. Soc.*, 165, A104 (2018)]

S. Hildebrand,[1,2] A. Rheinfeld,[3] A. Friesen,[1] J. Haetge,[1] F. M. Schappacher,[1] A. Jossen,[3] and M. Winter[1,2,4]

[1]*MEET Battery Research Center, Westfälische Wilhelms-Universität Münster, D-48149 Münster, Germany*
[2]*Institute of Physical Chemistry, Westfälische Wilhelms-Universität Münster, D-48149 Münster, Germany*
[3]*Institute for Electrical Energy Storage Technology, Technical University of Munich, D-80333 Munich, Germany*
[4]*Helmholtz-Institute Münster, IEK-12, Research Center Jülich GmbH, D-48149 Münster, Germany*

 [DOI: 10.1149/2.0851802jes] Published January 20, 2018.

Figure 2 on page A106 should appear as shown at right.

Equation 14 on page A113 should appear as

$$\frac{\mathrm{d}T}{\mathrm{d}t} = \frac{1}{C_{p,\mathrm{cell}}} \sum_i \left(m_i \cdot H_i \cdot \gamma_i \cdot e^{-\frac{E_{\mathrm{a},i}}{k_\mathrm{B} T}} \cdot (1-\alpha_i) \cdot (-\ln(1-\alpha_i))^{\frac{2}{3}} \right) \quad [14]$$

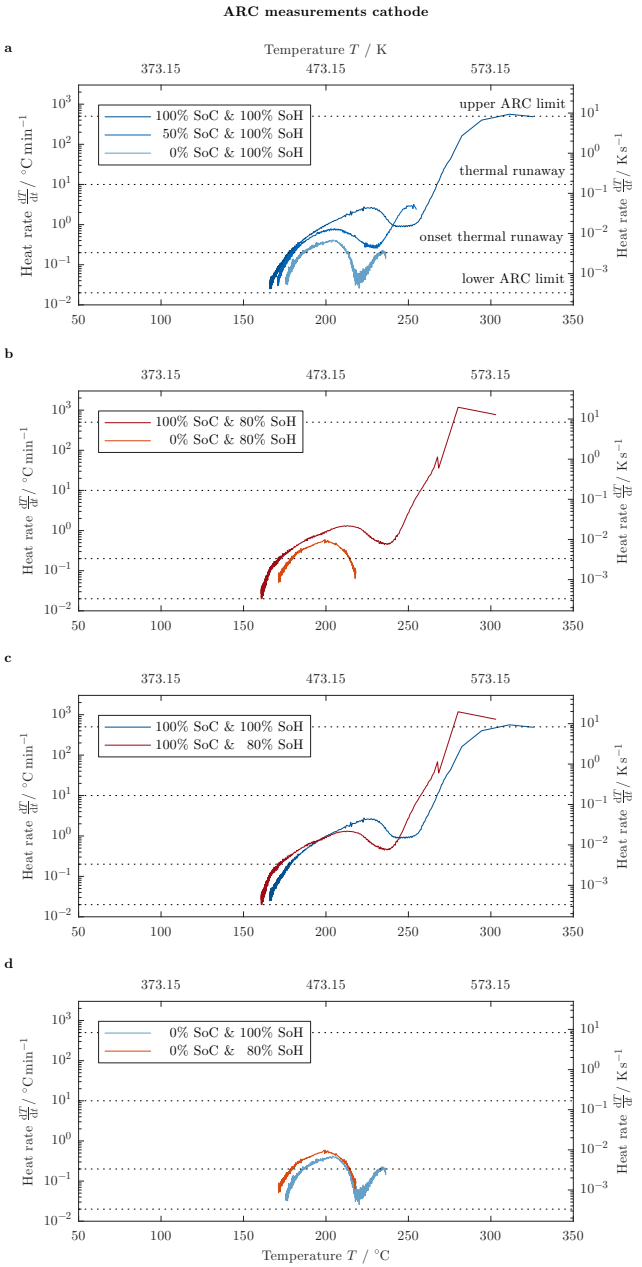

Figure 2. ARC-HWS results comparing the self-heating rate of NMC-442/electrolyte mixtures as a function of sample temperature indicating the SoC influence at 100% SoH (a), the SoC influence at 80% SoH (b), the impact of SoH at 100% SoC (c) and the impact of SoH at 0% SoC (d).